Published in Applied Optics, vol. 39, no. 25, pp. 4473-4485 (2000).

Angular distribution of light scattered from a sinusoidal grating

Egon Marx, Thomas A. Germer, and Theodore V. Vorburger

National Institute of Standards and Technology

Gaithersburg, Maryland 20899 USA

and

Byong C. Park

Korean Research Institute of Standards and Science

P. O. Box 102, Yusong, Taejon, 305-600 Korea

ABSTRACT

The angular distributions of light scattered by gold-coated and aluminum-coated gratings having amplitudes of ~90 nm and periods of 6.67 µm were measured and calculated for light incident from a HeNe laser at an angle of 6°. Experimental results are compared with predictions of Beckmann's scalar theory and Rayleigh's vector theory. The measured scattering pattern has a background of scattered light due mainly to residual surface roughness. Also the power in the higher-order peaks is larger by several orders of magnitude than the computed one, which can be attributed mainly to the low-order contributions of the harmonics in the profile.

Keywords: BRDF instrument, harmonics, light scattering, residual roughness, sinusoidal grating, stylus instrument.

1. Introduction

Coherent light, when scattered from a sinusoidal grating, forms a pattern in the far field that shows diffraction peaks. The number of peaks and their positions are governed by the well-known grating formula. While the positions are determined by the period of the grating and the angle of incidence, the power in the peaks depends mainly on the amplitude of the grating.

Laser light scattering from a holographic grating has been investigated with a view toward its possible use in the determination of the linearity of bidirectional reflectance distribution function (BRDF) instruments, a task that requires a wide dynamic range in scattering power, over seven orders of magnitude or more. When the amplitude of the grating is much smaller than the wavelength of the laser light, the power in the peaks decreases rapidly as the order increases, giving rise to the desired large range of power values. Another possible advantage of this approach is that the power for the diffraction orders might be predicted and controlled through the designed groove shape, that is, the amplitudes and relative phases of the fundamental and harmonic components of the grating profile. In addition, it might be possible to predict the power in the peaks by measuring the profiles of the grating grooves.

In this paper we report on measurements of the BRDF of two samples of sinusoidal surfaces and on the theory that we used to analyze scattering by perfect sinusoids and by surfaces described by a measured profile. The experimental scattering pattern differs significantly from that predicted by approximate theories applied to perfectly conducting sinusoidal surfaces, such as the Beckmann scalar theory and the Rayleigh vector theory. The background scattering is much lower and the power in the higher-order peaks is much larger than predicted. We come to the conclusion that the reduction of the background scattering is due to the two-dimensional

nature of the residual surface roughness and that the power in the higher-order peaks is explained by harmonics in the profile.

The scattering of light emitted by a CO_2 laser (wavelength $\lambda = 10.6$ µm) from a diamond-turned sinusoidal grating (NIST SRM 2071: amplitude a ≈ 0.5 µm, period D ≈ 100 µm) was previously described.[1-3] The analysis indicated that a step window contributed to the large computed background scattering which obscured the higher-order peaks, while other windows that represent more realistic beam profiles led to better results. Furthermore, it was found that harmonics of the profile caused peaks to appear above the background at the locations of the higher-order peaks and that the residual roughness did not affect the results in a significant manner.

Here we analyze the HeNe laser light ($\lambda = 0.6328$ µm) scattered by a pair of holographic gratings (amplitude a ≈ 90 nm, period D ≈ 6.67 µm) and our results differ from those obtained for the CO_2 laser. The residual roughness, rather than the step window, is found to cause a large computed scattering background. The effect of the windowing function is too small to affect significantly the computed scattering background. We propose that harmonics of the profile explain the relatively large amplitude of the higher-order diffraction peaks, but amplitudes and phases of the harmonics cannot be obtained directly from the measured profiles by a least-squares fit of the first terms of a Fourier series mainly because the point-to-point spacing fluctuates.

Some of the preliminary conclusions drawn from this investigation[4] have changed. New scattering measurements carried out on similar samples show that the difference between scattering of s- and p-polarized light is much smaller than that reported in Ref. 4. The previous

discrepancy was probably caused by misalignment of the sample. Also the dependence of the power in the peaks on the phases of harmonics is now properly taken into account in derivations within the Beckmann theory. Some preliminary results found in Ref. 4 that remain valid are quoted here without further elaboration.

The equations for the intensity of the light scattered by a sinusoidal grating obtained using the Beckmann and Rayleigh theories for a perfect conductor, as well as a discussion of harmonics and residual roughness, are presented in Sec. 2. Experimental results and comparison with computations are found in Sec. 3 and results are summarized in Sec. 4.

2. Theory

There are a number of theoretical definitions and derivations that are needed to discuss the experiments carried out with the sinusoidal surfaces. In Sec. 2.A we sketch the derivation of the Beckmann theory of scalar wave scattering by perfect conductors, in Sec. 2.B we give the formulas for the diffracted power for the two polarizations of the incident light in the Rayleigh theory, in Sec. 2.C we derive equations for the effects of the residual roughness of the sinusoidal surface, and in Sec. 2.D we briefly describe how the harmonic content of a profile can in principle be determined.

A. Beckmann Theory

We first assume that a plane wave is incident upon a perfectly conducting sinusoidal specimen with no harmonics and no residual roughness. The profile for such a surface is

$$h(x) = a\sin(Kx + \alpha)\,, \tag{1}$$

where a is the amplitude, K is the spatial wavenumber given by $2\pi/D$, D is the period, and α is a phase constant.

Beckmann[5] solved the scattering problem by using the scalar wave equation and the Kirchhoff approximation. For a one-dimensionally rough surface, the angular distribution of the scattered field at a large distance from the illuminated part of the surface, normalized to the field that is obtained in the specular direction for a smooth surface, is given by[6]

$$\rho(\theta_i,\theta_s) = [F(\theta_i,\theta_s)/L]\int_{-½L}^{½L} dx\,\exp[ixv_x(\theta_i,\theta_s) + ih(x)v_z(\theta_i,\theta_s)]\,, \tag{2}$$

where θ_i and θ_s are the incidence and scattering angles, respectively, $v_x = k(\sin\theta_i - \sin\theta_s)$, $v_z = -k(\cos\theta_i + \cos\theta_s)$, k is the optical wavenumber $2\pi/\lambda$, L is the width of the illuminated area on the sample, assumed here to be infinite in the other direction, and edge terms have been neglected. See Fig. 1 for definitions and sign conventions of the parameters.[7] The obliquity factor, $F(\theta_i,\theta_s)$, is given by

$$F(\theta_i,\theta_s) = (1 + \cos\theta_i\cos\theta_s - \sin\theta_i\sin\theta_s)/[\cos\theta_i(\cos\theta_i + \cos\theta_s)]\,. \tag{3}$$

We use the Jacobi-Anger expansion of an exponential in terms of Bessel functions,

$$\exp(i\Delta\sin\xi) = \sum_{n=-\infty}^{\infty} J_n(\Delta)\exp(in\xi)\,, \tag{4}$$

set $\Delta(\theta_i,\theta_s) = av_z(\theta_i,\theta_s)$ and $\xi = Kx + \alpha$, and substitute this expansion into Eq. (2) to obtain

$$\rho(\theta_i,\theta_s) = [F(\theta_i,\theta_s)/L]\int_{-½L}^{½L} dx \exp[ixv_x(\theta_i,\theta_s)] \sum_{n=-\infty}^{\infty} J_n[\Delta(\theta_i,\theta_s)] \exp[in(Kx + \alpha)] . \tag{5}$$

We integrate each term of the sum and get

$$\rho(\theta_i,\theta_s) = F(\theta_i,\theta_s) \sum_{n=-\infty}^{\infty} \exp(in\alpha) J_n[\Delta(\theta_i,\theta_s)] \operatorname{sinc}\{½L[v_x(\theta_i,\theta_s) + nK]\} . \tag{6}$$

The maxima of the sinc functions occur when $v_x + nK = 0$, which is satisfied for the finite set of values of θ_s that are the real solutions of the grating equation,

$$\sin\theta_n - \sin\theta_i = n\lambda/D, \quad n = -N_1, -N_1 + 1, ..., N_2 . \tag{7}$$

Multiplying ρ in Eq. (6) by its complex conjugate, we obtain

$$|\rho(\theta_i,\theta_s)|^2 = [F(\theta_i,\theta_s)]^2 \sum_{n=-\infty}^{\infty} \{J_n[\Delta(\theta_i,\theta_s)]\}^2 \operatorname{sinc}^2\{½L[v_x(\theta_i,\theta_s) + nK]\} , \tag{8}$$

where we have assumed that, if L » D, the diffraction peaks are very narrow and the field of one peak is almost zero at the positions of the other peaks, so that products of terms of different order are negligible. The sum can be restricted to the physical values of n in Eq. (7) because the contributions of the other terms in the infinite sum are negligible.

We assume that the full detection aperture angle, θ_A, is much larger than the width of the peak, whence the value of the detected power is essentially constant within the range of the aperture. The power distribution, up to a constant factor, can then be expressed by

$$P(\theta_i,\theta_s) \propto \sum_{n=-N_1}^{N_2} F^2(\theta_i,\theta_n) J_n^2[\Delta(\theta_i,\theta_n)] \mathrm{rect}[(\theta_s - \theta_n)/\theta_A] , \tag{9}$$

where the rectangle function rect(x) is 1 if $|x| < ½$ and 0 otherwise. Bessel functions decrease rapidly with the order n. This expression for the power in the diffraction peaks is what the Beckmann theory predicts. Stover[8] computes the power contained in the diffraction peak of order n for a sinusoidal grating and obtains $P_i J_n^2[\Delta(\theta_i,\theta_n)]\cos^2(\theta_n)$ in terms of the incident power, P_i, which shares the rapidly varying function of θ_n, $J_n^2(\Delta)$, with the terms in Eq. (9).

If we allow the sinusoidal grating to have M harmonics, the profile has the form

$$h(x) = \sum_{m=1}^{M} a_m \sin(K_m x + \alpha_m) , \quad K_m = mK . \tag{10}$$

Instead of Eq. (2) we obtain the scattering coefficient

$$\rho(\theta_s) = [F(\theta_s)/L] \int_{-½L}^{½L} dx \exp\left\{ ixv_x(\theta_s) + i\left[\sum_{m=1}^{M} a_m \sin(K_m x + \alpha_m) \right] v_z(\theta_s) \right\}$$

$$= [F(\theta_s)/L] \int_{-½L}^{½L} dx \exp[ixv_x(\theta_s)] \prod_{m=1}^{M} \exp[ia_m \sin(K_m x + \alpha_m) v_z(\theta_s)] , \tag{11}$$

where the dependence on θ_i is left implicit for conciseness. We use again the expansion in Eq. (4) for each term in the product and obtain

$$\rho(\theta_s) = [F(\theta_s)/L] \int_{-½L}^{½L} dx \exp[ixv_x(\theta_s)] \prod_{m=1}^{M} \left\{ \sum_{n_m=-\infty}^{\infty} J_{n_m}[\Delta_m(\theta_s)] \exp[in_m(K_m x + \alpha_m)] \right\} , \tag{12}$$

where $\Delta_m(\theta_s) = a_m v_z(\theta_s)$. We carry out the multiplication, which means that the product of the sums becomes a sum of the products, and obtain

$$\rho(\theta_s) = F(\theta_s) \sum_{n_1=-\infty}^{\infty} \sum_{n_2=-\infty}^{\infty} \ldots \sum_{n_M=-\infty}^{\infty} \exp[i\alpha(\nu)] J_{n_1}[\Delta_1(\theta_s)] J_{n_2}[\Delta_2(\theta_s)] \ldots J_{n_M}[\Delta_M(\theta_s)] \mathrm{sinc}\{½L[v_x(\theta_s) + N(\nu)K]\} , \tag{13}$$

where ν stands for the set of indices and

$$\alpha(\nu) = \alpha(n_1, \ldots, n_M) = \sum_{m=1}^{M} n_m \alpha_m , \qquad N(\nu) = N(n_1, \ldots, n_M) = \sum_{m=1}^{M} m\, n_m . \tag{14}$$

The peaks of the sinc functions in Eq. (13) occur at the values of N that make the argument vanish, that is, for N equal to the values of n that satisfy the grating equation. We use δ_{ij} for the Kronecker delta, which is equal to 1 when i = j and vanishes otherwise. We group together the terms that have the same value of N and rewrite Eq. (13) as

$$\rho(\theta_s) = F(\theta_s) \sum_{n=-\infty}^{\infty} \mathrm{sinc}\{½L[v_x(\theta_s) + nK]\} \rho_n(\theta_s) , \tag{15}$$

where

$$\rho_n(\theta_s) = \sum_{n_1=-\infty}^{\infty} \sum_{n_2=-\infty}^{\infty} \ldots \sum_{n_M=-\infty}^{\infty} \delta_{nN(\nu)} \exp[i\alpha(\nu)] J_{n_1}[\Delta_1(\theta_s)] J_{n_2}[\Delta_2(\theta_s)] \ldots J_{n_M}[\Delta_M(\theta_s)] . \tag{16}$$

Each ρ_n is made up of a sum of terms that correspond to different order peaks of the fundamental

and the harmonics, each multiplied by a phase factor given by the corresponding $\alpha(\nu)$. If the products of sinc functions of different arguments are negligible, the intensity is proportional to

$$|\rho(\theta_s)|^2 = [F(\theta_s)]^2 \sum_{n=-\infty}^{\infty} \mathrm{sinc}^2\{\tfrac{1}{2}L[v_x(\theta_s) + nK]\}|\rho_n(\theta_s)|^2 . \tag{17}$$

The power as a function of scattering angle is obtained as before, and we get

$$P(\theta_s) \propto \sum_{n=-N_1}^{N_2} [F(\theta_n)]^2 \,\mathrm{rect}[(\theta_s - \theta_n)/\theta_A]\,|\rho_n(\theta_n)|^2 . \tag{18}$$

This equation gives the power in the diffraction peaks when the grating profile contains harmonics of the fundamental sinusoid.

If we set h(x) = 0 in Eq. (2), we obtain a field amplitude proportional to a sinc function with slowly decreasing oscillations for scattering angles of increasing magnitude. This behavior, which extends to surfaces with a root-mean-square (rms) roughness small compared to the wavelength of the incident light, does not correspond to that of measured power distributions and is a consequence of the step windowing function assumed in the Kirchhoff approximation. An incident field that is of constant amplitude over the illuminated region and drops discontinuously to zero outside was found to lead to difficulties[2,3] that do not occur when a better behaved beam profile is used. We thus multiply the integrand in Eq. (2) by a windowing function, W(x), and obtain

$$\rho(\theta_s) = F(\theta_s)\int_{-\infty}^{\infty} dx\, W(x) \exp[ixv_x(\theta_s) + ih(x)v_z(\theta_s)] . \tag{19}$$

We have removed the factor 1/L, which affects only the normalization, and we have extended the range of integration to infinity by assuming that W(x) vanishes at large distances. We tried a Gaussian, a cosine, a sinc, and a Schwartz windowing function. We prefer the Schwartz function, defined by

$$W(x) = \begin{cases} \exp[-\alpha x^2/(L^2 - x^2)], & |x| \le L, \\ 0, & \text{elsewhere}, \end{cases} \tag{20}$$

where α is a parameter. This function is infinitely differentiable and vanishes outside a finite interval of length 2L. The actual beam profile, apertures, and other characteristics of the instrument are more accurately represented by a measured signature or response function, which can then be convolved with the computed intensity distribution. A more accurate representation of the beam cross section would require that we formulate the problem in three dimensions because the illuminated spot is finite. It would also be more accurate to use a complex, as opposed to real, windowing function.

B. Rayleigh Theory

The Rayleigh vector theory, which applies to perfectly conducting gratings, provides the power in the diffracted peaks for different incident polarizations.[9] The power in the nth order diffraction peak relative to the specular power, P_n, is given by

$$P_n = (\beta_n/\beta)|B_n|^2, \quad \beta_n = \sqrt{k^2 - \alpha_n^2}, \quad \alpha_n = k\sin\theta_i + Kn, \quad \beta = \beta_0 = k\cos\theta_i, \tag{21}$$

where the B_n are determined by the matrix equation

$$\sum_{n=-\infty}^{\infty} a_{mn} B_n = h_m, \quad m = 0, \pm 1, \pm 2, \ldots. \tag{22}$$

The a_{mn} and h_m are given in terms of the Bessel functions, J_n, and the modified Bessel functions of the first kind, I_n, by

$$a_{mn} = \begin{cases} i^{m-n} D J_{m-n}(\beta_n a) & \text{if } \beta_n^2 \geq 0, \\ (-1)^{m-n} D I_{m-n}(|\beta_n| a) & \text{if } \beta_n^2 < 0, \end{cases} \tag{23}$$

$$h_m = -(-i)^m D J_m(\beta a), \tag{24}$$

for the incident electric field perpendicular to the plane of incidence, s polarization, and

$$a_{mn} = \begin{cases} i^{m-n} \{ \pi a \alpha_n [-J_{m-n-1}(\beta_n a) - J_{m-n+1}(\beta_n a)] + D\beta_n J_{m-n}(\beta_n a) \} & \text{if } \beta_n^2 \geq 0, \\ (-1)^{m-n} \{ i\pi a \alpha_n [I_{m-n-1}(|\beta_n| a) - I_{m-n+1}(|\beta_n| a)] + D\beta_n I_{m-n}(|\beta_n| a) \} & \text{if } \beta_n^2 < 0, \end{cases} \tag{25}$$

$$h_m = (-1)^{m+1} i^m \{ \pi a \alpha_0 [J_{m-1}(\beta a) + J_{m+1}(\beta a)] + D\beta J_m(\beta a) \}, \tag{26}$$

for the incident electric field in the plane of incidence, p polarization. In practice we limit the values of m and n in Eq. (22) to a finite set.

C. Scattering Due to the Residual Roughness

We now consider the effect of the residual roughness on the background scattering based on the Beckmann theory for the one-dimensional case. The profile,

$$h(x) = a\sin(Kx + \alpha) + h_r(x), \tag{27}$$

includes a function $h_r(x)$ that represents the random roughness. Then the scattering amplitude is given by Eq. (19), which becomes

$$\rho(\theta_s) = F(\theta_s)\int_{-\infty}^{\infty} dx\, W(x)\exp[i\,x\,v_x(\theta_s) + i\,a\sin(Kx + \alpha)v_z(\theta_s) + i\,h_r(x)v_z(\theta_s)]\,. \tag{28}$$

We choose a Gaussian window,

$$W(x) = \left(\sqrt{2\pi}\,w\right)^{-1}\exp\left[-\,x^2/(2w^2)\right], \tag{29}$$

because the Gaussian function can be more easily treated mathematically and it allows us to extend the range of integration. We obtain

$$\langle|\rho(\theta_s)|^2\rangle = [F(\theta_s)]^2\sum_{n=-\infty}^{\infty}\sum_{n'=-\infty}^{\infty}\exp[i(n-n')\alpha]J_n[\Delta(\theta_s)]J_{n'}[\Delta(\theta_s)]\,[1/(2\pi w^2)]\int_{-\infty}^{\infty}dx\int_{-\infty}^{\infty}dx'$$
$$\cdot\exp\left\{-\,(x^2 + x'^2)/(2w^2) + i[(x - x')v_x(\theta_s) + K(nx - n'x')]\right\}\langle\exp\{i[h_r(x) - h_r(x')]v_z\}\rangle, \tag{30}$$

where the angular brackets indicate an ensemble average. We further assume that the height distribution and the autocorrelation function of the residual roughness are Gaussian. The residual roughness is characterized by its rms value σ and autocorrelation length T. Then the ensemble average is[10]

$$\langle \exp\{iv_z[h_r(x) - h_r(x')]\}\rangle = \exp(-g)\exp[gC(R)], \tag{31}$$

where $g = v_z^2\sigma^2$, $C(R) = \exp(-R^2/T^2)$, and $R = x - x'$. We substitute this ensemble average into Eq. (30) and integrate. Since most surfaces have parameters that satisfy $w \gg T$ and $g \ll 1$, we expand functions of g to first order and drop terms proportional to $(T/w)^2$. In Eq. (30), the term with the exponent proportional to K leads to a factor $\exp[-\frac{1}{4}(n - n')^2(2\pi w/D)^2]$, which is negligible compared to 1 if $n \neq n'$ because w is generally greater than several D. We then obtain

$$\begin{aligned}\langle|\rho(\theta_s)|^2\rangle \approx [F(\theta_s)]^2 \sum_{n=-\infty}^{\infty} J_n[\Delta(\theta_s)]^2 \Big\{ &(1 - g)\exp\Big[-w^2\big(v_x(\theta_s) + nK\big)^2\Big] \\ &+ g(T/2w)\exp\Big[-\tfrac{1}{4}T^2\big(v_x(\theta_s) + nK\big)^2\Big]\Big\}.\end{aligned} \tag{32}$$

The second term is associated with the power spectral density (PSD) of the residual roughness. The PSD of the random Gaussian component of the profile, $S(f_x)$, is given by the Fourier transform of the unnormalized autocorrelation function, that is,

$$\begin{aligned}S(f_x) &= \int_{-\infty}^{\infty} dR \exp(-2\pi i f_x R)\sigma^2 C(R) = \int_{-\infty}^{\infty} dR \exp(-2\pi i f_x R)\sigma^2 \exp(-R^2/T^2) \\ &= \sigma^2\sqrt{\pi}T\exp(-\pi^2 f_x^2 T^2).\end{aligned} \tag{33}$$

Thus, in this particular case, Eq. (32) can be written in terms of $S(f_{nx})$,

$$\langle|\rho(\theta_s)|^2\rangle \approx \sum_{n=-\infty}^{\infty} J_n[\Delta(\theta_s)]^2 \Big\{(1 - g)\exp\Big[-w^2\big(v_x(\theta_s) + nK\big)^2\Big] + \big(v_z(\theta_s)^2/2\sqrt{\pi}w\big)S(f_{nx})\Big\}, \tag{34}$$

where

$$f_{nx} = [v_x(\theta_s) + nK]/(2\pi) = (\sin\theta_n - \sin\theta_s)/\lambda . \tag{35}$$

Equation (34) can be interpreted as follows: the diffraction peak and its window-induced tails are attenuated by a factor $1-g$, while the background is generated by a term proportional to the PSD of the residual roughness. Let us call this PSD term the residual roughness tail for convenience. From Eq. (32) we can see that the residual roughness tail is a slowly decreasing function of f_x which has a small peak value, $gT/2w$, that determines the magnitude of the background scattering, while the windowing tail is a rapidly decreasing function with a relatively large peak value, $1 - g$. These results should not depend strongly on the choices of a Gaussian windowing function, height distribution, and autocorrelation function.

Actually, the residual roughness is two-dimensional in nature even though the main grating profile is one-dimensional. Consequently, Eq. (27) should be replaced by

$$h(x,y) = a\sin(Kx + \alpha) + h_r(x,y). \tag{36}$$

We assume that the azimuthal angle of the direction of incidence is equal to zero and we introduce the azimuthal angle, φ_s, of the scattering direction and obtain the two-dimensional analogue of Eq. (28),

$$\rho(\theta_s,\varphi_s) = F_3(\theta_s,\varphi_s)\int_{-\infty}^{\infty}\int_{-\infty}^{\infty} dxdy\, W(x,y)\exp\{i[xv_x(\theta_s,\varphi_s) + yv_y(\theta_s,\varphi_s)$$
$$+ a\sin(Kx + \alpha)v_z(\theta_s) + h_r(x,y)v_z(\theta_s)]\} , \tag{37}$$

where $v_x = k(\sin\theta_i - \sin\theta_s\cos\varphi_s)$, $v_y = k\sin\theta_s\sin\varphi_s$, and

$$F_3(\theta_s,\varphi_s) = (1 + \cos\theta_i\cos\theta_s - \sin\theta_i\sin\theta_s\cos\varphi_s)/[\cos\theta_i(\cos\theta_i + \cos\theta_s)] . \tag{38}$$

We replace W(x) defined in Eq. (29) with

$$W(x,y) = (2\pi w^2)^{-1}\exp[-(x^2 + y^2)/(2w^2)] . \tag{39}$$

A lengthy calculation leads to the analogue of Eq. (32), namely

$$\langle|\rho(\theta_s,\varphi_s)|^2\rangle \approx [F_3(\theta_s,\varphi_s)]^2 \sum_{n=-\infty}^{\infty} J_n[\Delta(\theta_s)]^2\Big\{(1 - g)\exp\Big[-w^2\big(v_x(\theta_s,\varphi_s) + nK\big)^2 - w^2 v_y(\theta_s,\varphi_s)^2\Big]$$
$$+ g(T_x T_y/4w^2)\exp\Big[-\tfrac{1}{4}T_x^2\big(v_x(\theta_s,\varphi_s) + Kn\big)^2 - \tfrac{1}{4}T_y^2 v_y(\theta_s,\varphi_s)^2\Big]\Big\} , \tag{40}$$

where T_x and T_y are the corresponding Gaussian roughness autocorrelation lengths. We can now express the intensity in terms of the two-dimensional PSD,[11] $S(f_x,f_y)$, by

$$\langle|\rho(\theta_s,\varphi_s)|^2\rangle \approx [F_3(\theta_s,\varphi_s)]^2 \sum_{n=-\infty}^{\infty} J_n[\Delta(\theta_s)]^2\Big\{(1 - g)\exp\Big[-w^2\big(v_x(\theta_s,\varphi_s) + nK\big)^2 - w^2 v_y(\theta_s,\varphi_s)^2\Big]$$
$$+ [v_z(\theta_s)^2/(4\pi w^2)]\, S(f_{nx}, f_y)\Big\} , \tag{41}$$

where f_{nx} is unchanged and $f_y = \sin\theta_s\sin\varphi_s/\lambda$. This equation will then result in a much lower background due to the residual roughness than Eq. (34) when the intensity distribution is determined in the plane of incidence because for one-dimensional roughness all the light is scattered in that plane. The measured quantity is the power, or the intensity integrated over the finite size detector aperture, which corresponds to the integral of the intensity in Eq. (41) with

respect to f_x and f_y. Since the residual roughness is very small compared to the wavelength of light, the distribution of the scattered intensity perpendicular to the plane of incidence is proportional to the PSD along the f_y-axis, so that the limits of integration are determined by the aperture size. The integration has to be carried out from $-f_1$ to f_1, where $f_1 = \sin(\frac{1}{2}\theta_A)/\lambda$. For isotropic residual roughness we have $S(f_x,f_y) = S_2(f)$, where $f = \sqrt{f_x^2 + f_y^2}$, and the ratio of the background intensities of the actual surface to a one-dimensionally rough surface is

$$R_{back} = \int_0^{f_1} df_y \; S_2\left(\sqrt{f_x^2 + f_y^2}\right) \Big/ \int_0^{\infty} df_y \; S_2\left(\sqrt{f_x^2 + f_y^2}\right). \tag{42}$$

A rigorous vector theory[12] which takes into account both finite conductivity and polarization effects could be used to calculate the scattered light. We have used instead the approximate Rayleigh theory to determine the difference between polarizations. The approximation is valid for $ka < 0.448$, as determined by comparison with the rigorous theory in the case of the sinusoidal grating.[13] For the present problem we have $ka \approx 0.075$, which is included in the range of validity. The Rayleigh theory assumes, however, a perfectly conducting scatterer.

D. Harmonics

A profile of a nominally sinusoidal surface is likely to contain harmonics of the fundamental sinusoid and a part that is not periodic called the residual roughness. One method to determine these harmonics consists in expanding a measured profile h(x) into a truncated Fourier series

$$h(x) \approx \tfrac{1}{2}A_0 + \sum_{m=1}^{M}\left[A_m\cos(mKx) + B_m\sin(mKx)\right] = \tfrac{1}{2}A_0 + \sum_{m=1}^{M} a_m\sin(mKx + \alpha_m)\,, \qquad (43)$$

where the coefficients can be obtained by integration from

$$A_n = \frac{K}{\pi N_p}\int_0^L dx\, h(x)\cos(nKx)\,, \quad n = 0,\ 1,\ 2,\ldots\,, \qquad (44)$$

$$B_n = \frac{K}{\pi N_p}\int_0^L dx\, h(x)\sin(nKx)\,, \quad n = 1,\ 2,\ldots\,, \qquad (45)$$

where $L = N_pD$, assuming that the length, L, is an integer multiple of the period, D. If a linear trend is removed from the data, the coefficient A_0 vanishes. The period can be determined by a least-squares fit of a sinusoid with the assumed number of harmonics to the profile. As the period varies, the part of the profile that corresponds to an integer number of periods changes too, and has to be adjusted at each step of the minimization.

An alternative determination of the harmonic content of the periodic surface is the computation of the PSD.[4] The amplitude of a harmonic can be estimated from the magnitude of the peak in the PSD at the corresponding frequency, but we do not obtain the information on the corresponding phase.

3. Experimental and Computed Results

We have used aluminum- and gold-coated holographic gratings manufactured by the American Holographic Co.[14] The samples used in the experiments reported here are not those used in our previous work,[4] although they have the same nominal dimensions.

In Sect. 3.A we describe the stylus measurements and the profiles obtained from the samples as well as a partial determination of its harmonic content. In Sect. 3.B we present the results of BRDF measurements and comparisons with computations based on measured profiles, including the effects of residual roughness.

A. Stylus Measurements

Surface profiles were obtained using a Talystep stylus profilometer with a 1 μm radius tip at the same centered spot where light scattering measurements were performed. We obtained three 1 mm profiles in a line and two more at a distance of 1 mm to the side of the central profile. Each profile had 12000 points. We previously found[4] that the use of a 0.1 μm radius tip did not lead to significantly different results. The profilometer was calibrated before and after these measurements for both horizontal and vertical displacements. We estimate that the error in the vertical displacement is ~1%. The measured profiles show occasional large excursions or outliers, which we attribute to particle contamination and scratches. We determined the amplitude of the sinusoid by first subtracting the linear trend of the profile by a least-squares-fit method and then computing the root-mean-square deviation from the baseline. We multiply the result by $\sqrt{2}$ to obtain an approximate value of the amplitude. The average of the calculated amplitudes obtained in this manner from the five profiles is 0.0945 μm for the aluminum

specimen and 0.0902 μm for the gold specimen. Outliers in the profiles for the aluminum specimen make the calculated amplitudes vary from 0.0861 μm to 0.1114 μm. Outliers that correspond to defects in the surface clearly do not extend to infinity, thus affecting the measured scattering intensities much less than the scattering calculated for a surface that varies only in one dimension.

The magnitude and phase of the lower-order harmonics can in principle be obtained by the procedure outlined in Sect. 2.D. However, when this procedure is carried out, results show that the apparent period of the measured profile varies, leading to a poor least-squares fit of a periodic function. The fitted periodic function and the measured profile are often out of phase, which adds large contributions to the quality of fit function. This drift is probably due to a variation in the speed of the stylus motion across the sample and not to an actual period variation. To correct for the stylus speed variations we changed the horizontal coordinates to make the zero-crossings equispaced and the period equal to 6.67 μm using a cubic spline interpolation. Periods that contained outliers were deleted and 100 periods of the new profile were digitized at constant point-to-point-spacing by means of another cubic spline interpolation. These corrected profiles are then used in the BRDF calculations described in the next Section. Variations in amplitude have a less drastic effect on the least-squares fit.

The amplitudes computed for the corrected profiles vary between 81.7 nm and 87.8 nm, averaging 83.9 nm, for the aluminum sample, and between 85.7 nm and 90.5 nm, averaging 88.1 nm, for the gold sample. Consequently we decided to use a value of 86 nm in calculations for a perfect sinusoid, which is an idealized representation of the actual surface. The discrepancy by several orders of magnitude for the higher-order peaks is not affected significantly by small

changes in the amplitude. The values of the computed diffraction peak angles for an angle of incidence of 6°, as well as measured and computed power in the peaks, are given in Table 1.

Part of one of the modified profiles of the gold sample is shown in Fig. 2a, where we can see that the amplitude of the profile varies significantly. This is typical of all of the measured profiles. The PSD of this profile is shown in Fig. 2c. A consequence of the modification is a narrowing of the peaks and an increase in their height. The second harmonic has an amplitude equal to ~4.5% of the fundamental, and the amplitudes of the peaks at the location of the fourth and fifth harmonics are ~1% and ~0.7% of the fundamental, respectively. There is no clear evidence of the third harmonic and peaks at higher spatial frequencies are not located at multiples of the fundamental frequency. The precise effect of the modification of the profiles on the harmonic content is unclear. Setting equal to zero the amplitude of the Fourier transform of the profile below a frequency of 0.33 μm^{-1} leads to the PSD in Fig. 2d, and the inverse Fourier transform gives a computed residual roughness that is missing the low spatial frequency components. A segment of this residual roughness is shown in Fig. 2b.

B. BRDF Measurements and Computations

We measured the BRDF for laser light incident on a centered spot on each of the two samples with both s and p polarization. We used a BRDF instrument, the Goniometric Optical Scatter Instrument (GOSI),[15,16] with a circular aperture angle, θ_A, of 0.7°, a scanning step angle of 0.5°, a convergence angle of the incident light of ~1°, and a spot size of ~1 mm in diameter. The BRDF is defined by

$$\text{BRDF} = \frac{\text{radiance}}{\text{irradiance}} \approx \frac{dP_s/d\Omega_s}{P_i\cos\theta_s} \approx \frac{P_s/\Omega_s}{P_i\cos\theta_s}, \tag{46}$$

where the indices *i* and *s* stand for incidence and scattering, respectively, P is the power, and θ_s is the polar angle of the scattering direction, and Ω_s is the solid angle. Figs. 3 and 4 show the results of these measurements, which do not exhibit the apparent dependence on polarization previously found.[4] The measured BRDF actually corresponds to the convolution of the function defined in Eq. (46) with the instrument signature, which reduces the magnitude of the peaks relative to the background.

The measured power in the diffraction peaks relative to the power in the specular peak, shown in the graphs in Figs. 3 and 4, are found in Table 1. They are compared to the corresponding computed results obtained from the Beckmann theory, using Eq. (9) for the perfect sinusoid and Eq. (19) for measured profiles, and from the Rayleigh theory using Eq. (21). The power differs from the BRDF by a constant factor and by the $\cos\theta_s$ in the denominators in Eq. (46). For the perfect sinusoid the Rayleigh method gives essentially the same results as the Beckmann method, which differ significantly from the power in the peaks of the measured curves, especially for the higher orders. There also is little difference between the two polarizations, as seen also in Table 1. A discussion of limitations of this approach can be found in Ref. 17.

The complex dielectric constant of gold at $\lambda = 0.6328$ μm is 0.166 + 3.15i, and that of aluminum is 1.51 + 7.65i.[18] A finite-conductivity theory[12] might improve the agreement between computed and measured BRDFs. For a perfect sinusoid of infinite extent illuminated by a plane

wave, all the power is concentrated in the direction of the diffraction peaks. On the other hand, the experimental data show substantial background scattering between the peaks. In addition, the measured power in the higher-order peaks is much larger than the power computed for a perfect sinusoid.

We consider two possible sources of the background scattering: the window that limits the incident beam and the residual roughness of the sinusoid. If the incident beam is truncated or has any spatial distribution other than plane wave, diffraction due to the beam profile or window will occur and may be significant. Also a realistic window would include the effects of the curvature of the phase front since the beam is converging at the sample and focused on the detector circle. It is difficult to represent the actual beam in a calculation, partly because the illuminated spot is not an infinite strip and solving a full three-dimensional scattering problem is much harder than the simplified problem we have addressed here. Nevertheless, we still need a windowing function in the integral in Eq. (19) because a step window gives rise to tails that decrease much more slowly than other windows.[2,3]

The instrument signature[19] shown in Fig. 5 was measured by scanning the 0.7 degree aperture across the beam in the absence of a sample. This signature is below 10^{-6} sr^{-1} for angles larger than 2° and is much smaller than the background scattering level measured with the holographic grating, shown in Figs. 3 and 4. Therefore, instrumental artifacts are not responsible for the background level measured between the diffraction peaks. Furthermore, since the instrument signature includes the effect of the physical window function [see Eq.(19) with h(x)=0] convolved with the 0.7 degree aperture, the physical window function does not contribute to the measured background scattering level either.

To include the effect of the residual roughness on the background scattering we have calculated the scattered intensity distribution numerically by using Eq. (19), substituting for h(x) the measured profiles corrected for the apparent distortion of the period. We have also used the Schwartz window defined in Eq. (20) with a parameter $\alpha = 0.1$ and a width L equal to the length of each profile. The physical aperture was taken into account by integrating the computed intensity over a 0.7° interval centered at the scattering angle. We average the five BRDF curves computed for the profiles taken on each sample and compare them to the measured BRDF curves for s-polarized light in Figs. 6 and 7, where we have matched the top of the specular peak of the computed BRDF to that of the measured one. The values of the peaks in the computed BRDF curves are also found in Table 1. Where the comparison is not obscured by the background in the calculated results, the correlation between the measured peak magnitudes and the calculated ones is good. The measured peaks are higher than the calculated peaks but not excessively so.

To gain some insight into the variation of the power in the peaks with the rms roughness we perform a numerical experiment and compare the computed power for one of the modified profiles obtained for the aluminum sample with that obtained from profiles that are scaled by increasing and decreasing the heights at all points by 5%. Variations in the height of the profiles are significantly larger than the 1% estimated error in the z-coordinates, as seen in Fig. 2. The results are shown in Table 2. To exhibit the variations in the power in the specular peak, we give the power in the peaks as fractions of the incident power. The changes in the power in the peaks of order 1 and -1 are much smaller than those of that in the specular peak because the parameters correspond to a maximum of $J_1(\Delta)$, so that variations are small. Since $J_0'(\Delta) = -J_1(\Delta)$, we have a maximum in the rate of change of the power in the specular peaks.

The magnitude of the measured peaks also depends on the location of the illuminated spot on the sample. To obtain the computed BRDF curves shown in Figs. 6 and 7 we were careful to measure the profiles at the same location as the illuminated spot used in the scatter measurements. We have also measured the light scattered by the surface at a number of neighboring spots. We again see that there is little variation of the first-order peaks, so to give an idea of the variation of the power in the peaks we show in Table 2 the values that correspond to the extremes of the power in the specular peak. Factors of ~2 in the higher-order peak power shown in Table 2 can be found both for the numerical experiment and the BRDF measurements.

The experimental background is much smaller than the computed one, which is due to the two-dimensional nature of the residual roughness. If we assume that the measured profile corresponds to a one-dimensionally rough surface, all the light scattered by the residual roughness is found in the plane perpendicular to the lay and is collected by the detector. Since the roughness actually is two-dimensional, only a fraction of the scattered light is collected by the detector. The integral of the PSD for frequencies less than $f_1 = 0.01\ \mu m^{-1}$ is proportional to the power scattered into the aperture. We note that the one-dimensional PSD, $S_1(f)$, of the measured profiles falls off approximately as $f^{-2.3}$ in the region of the higher frequencies that correspond to the residual roughness. This implies that the two-dimensional PSD of an isotropic surface, $S_2(f)$, falls off approximately as $f^{-3.3}$. We compute the power ratio for different values of θ_s using Eq. (42) with the value of f_x obtained from Eq. (35) for $n = 0$ and $\theta_i = 6°$, and we obtain the computed values found in Table 3. Comparison with the ratios obtained from the background portions of the curves shown in Figs. 6 and 7 agree well enough to conclude that the reduced background in the measured BRDF is due to the two-dimensional nature of the residual

roughness. The computed peak intensities should remain unchanged because the diffraction peaks are a consequence of the one-dimensional grating profile.

The Beckmann theory that has been commonly used to understand scattering experiments is a scalar theory that uses the Kirchhoff approximation. The limits of the validity of the Kirchhoff approximation for scattering from sinusoidal gratings has been discussed by Wirgin.[20] The intensities of the higher-order diffraction peaks for s-polarized light are similar for both specimens, and much larger than expected from the Beckmann theory for a perfect sinusoid.

The most likely reason for the discrepancy between the measured and computed magnitudes of the higher-order peaks is the presence of harmonics in the profile. The PSDs of the measured profiles clearly show several harmonics in addition to the fundamental. The first-order diffraction peak of the nth harmonic of the sinusoidal profile occurs at the same angle as the diffraction peak of order n of the fundamental sinusoid and the intensity due to the former may be much larger than that due to the latter.[2,3] A number of different harmonics can contribute to the same diffraction peak, as seen in Eq. (16). The background noise in the profile and the fluctuations in the stylus speed limit our ability to determine the higher-order harmonics in the samples, which could be used to compute the light scattered by a simulated profile without background noise. The calculations performed using the Beckmann theory on profiles obtained from stylus measurements do not show the intensities of the higher-order peaks above the computed background noise. The sharpness of the measured peaks in the BRDF curves indicates that the period of the sinusoids on the samples does not vary as much as indicated by the measured profiles.

4. Summary

We have investigated the scattering of laser light from two sinusoidal holographic gratings, one gold-coated and the other aluminum-coated. Measured and computed results are in reasonably good agreement for the lower-order peaks, as shown in Table 1.

These samples have limitations such as lack of homogeneity, residual roughness, and harmonic content that preclude their use to verify the linearity of BRDF instruments. The power scattered into the different peaks differs from the predictions using measured profiles by varying amounts to nearly a factor of two, as shown in Table 1. It is an open question whether the samples can be manufactured with sufficient uniformity of profile and sufficiently low residual roughness that reproducible measurements of peak intensities can be obtained over, say, seven orders of magnitude or more. The introduction of harmonics of predetermined amplitude and phase relative to the fundamental sinusoid could be used to produce peak intensities of different magnitudes.

The background in the measured BRDF is much smaller than the one computed via the Beckmann theory from the measured profiles. This is explained by the two-dimensional nature of the residual roughness, which is implicitly assumed to be one-dimensional in the calculation of the BRDF from the measured profile. Also the light beam profile can contribute to the background, but here we estimate that this contribution is negligible due to the sharpness of the instrument signature.

The magnitudes of the higher-order diffraction peak intensities are much larger than those predicted for a perfect sinusoid. We expect these peaks to arise from harmonics in the profile, but fluctuations in the speed of the stylus with respect to the sample, varying amplitude of the

sinusoid, possible distortion due to stylus tip shape, and background noise have kept us from finding their amplitudes and relative phases, although the amplitude of the second, fourth and fifth harmonics can be determined from the PSDs. However, it will be difficult to measure surface profiles with sufficient accuracy to calculate the weaker diffraction peaks accurately. Future work along these lines could include measurement of three-dimensional surface topography maps[21] that characterize the random roughness more correctly, which could then be used to compute the background scattering level.

We thank T. B. Renegar for the profilometer measurements.

References

1. E. Marx, T. R. Lettieri, T. V. Vorburger, and M. McIntosh, "Sinusoidal Surfaces as Standards for BRDF Instruments," in *Optical Scattering: Applications, Measurement, and Theory*, J. C. Stover, ed., Proceedings of the SPIE **1530**, 15-21 (1991).
2. E. Marx and T. V. Vorburger, "Windowing Effects on Light Scattered by Sinusoidal Surfaces," in *Optical Scattering: Applications, Measurement, and Theory II*, J. C. Stover, ed., Proceedings of the SPIE **1995**, 2-14 (1993).
3. E. Marx, T. R. Lettieri, and T. V. Vorburger, "Light Scattering by Sinusoidal Surfaces: Illumination Windows and Harmonics in Standards," Appl. Opt. **34**, 1269-1277 (1995).
4. B. C. Park, T. V. Vorburger, T. A. Germer, and E. Marx, "Scattering from sinusoidal gratings," in *Scattering and Surface Roughness*, Z.-H. Gu and A. Maradudin, eds., Proceedings of the SPIE **3141**, 65-77 (1997).

5. P. Beckmann and A. Spizzichino, *The Scattering of Electromagnetic Waves from Rough Surfaces* (Pergamon, New York, 1963), Chaps. 4 and 5.

6. J. A. Ogilvy, *Theory of Wave Scattering from Random Rough Surfaces* (Institute of Physics Publishing, Bristol, 1991), Chap. 4, pp. 80-84, .

7. See Ref. 6, p. 42.

8. J. C. Stover, *Optical Scattering: Measurement and Analysis* (McGraw-Hill, New York, 1990), p. 219.

9. R. Petit, "A Tutorial Introduction," in *Electromagnetic Theory of Gratings*, R. Petit, ed., (Springer-Verlag, Berlin, 1980), pp. 16-17.

10. See Ref. 5, p. 81, or Ref. 6, p. 89.

11. See Ref. 8, p. 60.

12. D. Maystre, "Integral Methods," in *Electromagnetic Theory of Gratings*, R. Petit, ed., (Springer-Verlag, Berlin, 1980), pp. 76-81.

13. G. R. Jiracek, "Numerical comparisons of a modified Rayleigh approach with other rough surface EM scattering solutions," IEEE Trans. Antennas Propagat. **21**, 393-396 (1973).

14. Certain commercial equipment is identified in this report to specify adequately the experimental procedure. In no case does such identification imply recommendation or endorsement by NIST, nor does it imply that the equipment identified is necessarily the best available for the purpose.

15. C. C. Asmail, C. L. Cromer, J. E. Proctor, and J. J. Hsia, "Instrumentation at the National Institute of Standards and Technology for bidirectional reflectance distribution function (BRDF) measurements," in *Stray Radiation in Optical Systems III*, R. P. Breault, ed.,

Proceedings of the SPIE **2260**, 52-61, (1994).

16. T. A. Germer and C. C. Asmail, "Goniometric optical scatter instrument for out-of-plane ellipsometry measurements," Rev. Sci. Instrum. **70**, 3688-3695 (1999).
17. J. E. Harvey, C. L. Vernold, A. Krywonos, and P. L. Thompson," Diffracted radiance: a fundamental quantity of nonparaxial scalar diffraction theory," Appl. Opt. **38**, 6469-6481 (1999).
18. E. D. Palik, *Handbook of Optical Constants* (Academic Press, San Diego, 1985), pp. 286-295 and 369-406.
19. See Ref. 8, pp. 112-115.
20. A. Wirgin, "Scattering from sinusoidal gratings: an evaluation of the Kirchhoff approximation," J. Opt. Soc. Am. **73**, 1028-1041 (1983).
21. D. A. Content, "Diffraction grating groove analysis used to predict efficiency and scatter performance," in *Gradient Index, Miniature, and Diffractive Optical Systems*, A. D. Kathman, Ed., Proceedings of the SPIE **3778**, 19-30 (1999).

Glossary of mathematical notation

a, D, K, α: amplitude, period, wavenumber, and phase of the sinusoid

$h(x)$, $h(x,y)$: surface profile

J_n, I_n: Bessel function and modified Bessel function of the first kind of order n

k, λ: wavenumber and wavelength of the laser light

L: width of illuminated strip

sinc: $\mathrm{sinc}\xi = \sin\xi/\xi$

$S(f_x)$, $S(f_x,f_y)$, $S_2(f)$: PSDs of a surface

v_x, v_y, v_z: components of the difference between the incident and scattered wavevectors

w: width of a Gaussian function

W: windowing function

ρ, P: electric field amplitude and power

θ_i, φ_i, θ_s, φ_s: polar and azimuthal angles of the incident and scattering directions (the azimuthal angle of the incident direction is assumed to vanish)

θ_n: angle for the diffraction peak of order n

σ, T, T_x, T_y: rms value and autocorrelation length(s) of residual roughness

Table 1. Measured and Computed Diffraction Peak Intensities Relative to the Specular Peak Intensity

Diffraction peak		Measured, aluminum[a]		Measured, gold[a]		Beckmann,[b] profiles		Beckmann,[c]	Rayleigh,[d] sinusoid	
order	angle	s-pol	p-pol	s pol	p pol	aluminum	gold	sinusoid	s pol	p pol
−11	−70.0°	—[e]	—[e]	—[e]	—[e]	—[g]	—[g]	5.68×10^{-20}	5.22×10^{-20}	6.19×10^{-20}
−10	−57.6°	—[e]	—[e]	—[e]	—[e]	—[g]	—[g]	1.87×10^{-16}	1.75×10^{-16}	2.01×10^{-16}
−9	−48.6°	1.10×10^{-6}	2.18×10^{-6}	5.58×10^{-7}	8.12×10^{-7}	—[g]	—[g]	1.42×10^{-13}	1.34×10^{-13}	1.50×10^{-13}
−8	−40.9°	5.22×10^{-6}	8.68×10^{-6}	1.89×10^{-6}	2.61×10^{-6}	—[g]	—[g]	4.66×10^{-11}	4.43×10^{-11}	4.90×10^{-11}
−7	−34.0°	2.21×10^{-5}	2.98×10^{-5}	6.76×10^{-6}	8.95×10^{-6}	—[g]	—[g]	8.25×10^{-9}	7.89×10^{-9}	8.63×10^{-9}
−6	−27.7°	5.16×10^{-5}	6.11×10^{-5}	2.01×10^{-5}	2.43×10^{-5}	—[g]	—[g]	8.62×10^{-7}	8.29×10^{-7}	8.96×10^{-7}
−5	−21.7°	5.84×10^{-5}	7.39×10^{-5}	2.13×10^{-4}	2.37×10^{-4}	3.40×10^{-4}	3.43×10^{-4}	5.47×10^{-5}	5.30×10^{-5}	5.66×10^{-5}
−4	−16.0°	2.59×10^{-3}	2.85×10^{-3}	4.67×10^{-3}	4.90×10^{-3}	2.13×10^{-3}	3.36×10^{-3}	2.09×10^{-3}	2.04×10^{-3}	2.16×10^{-3}
−3	−10.4°	—[f]	—[f]	—[f]	—[f]	4.08×10^{-2}	6.15×10^{-2}	4.59×10^{-2}	4.48×10^{-2}	4.70×10^{-2}
−2	−4.9°	—[f]	—[f]	—[f]	—[f]	0.406	0.585	0.508	0.499	0.517
−1	0.6°	2.35	2.46	2.77	2.84	1.78	2.36	2.11	2.08	2.13
0	6.0 °	1	1	1	1	1	1	1	1	1
1	11.5°	2.30	2.40	2.77	2.84	1.78	2.31	2.10	2.08	2.12
2	17.1°	0.583	0.626	0.728	0.753	0.377	0.562	0.478	0.469	0.487
3	22.9°	5.82×10^{-2}	6.49×10^{-2}	7.24×10^{-2}	7.61×10^{-2}	3.52×10^{-2}	5.63×10^{-2}	3.89×10^{-2}	3.80×10^{-2}	3.99×10^{-2}
4	29.0°	1.92×10^{-3}	2.10×10^{-3}	3.57×10^{-3}	3.80×10^{-3}	1.41×10^{-3}	2.75×10^{-3}	1.51×10^{-3}	1.47×10^{-3}	1.56×10^{-3}
5	35.4°	2.70×10^{-4}	2.99×10^{-4}	1.45×10^{-4}	1.61×10^{-4}	—[g]	3.10×10^{-4}	3.13×10^{-5}	3.01×10^{-5}	3.25×10^{-5}
6	42.4°	1.76×10^{-4}	2.24×10^{-4}	1.92×10^{-5}	2.38×10^{-5}	—[g]	—[g]	3.51×10^{-7}	3.35×10^{-7}	3.69×10^{-7}

7	50.3°	4.38×10^{-5}	7.41×10^{-5}	5.70×10^{-6}	8.38×10^{-6}	— [g]	— [g]	2.02×10^{-9}	1.90×10^{-9}	2.15×10^{-9}
8	59.8°	5.50×10^{-6}	1.33×10^{-5}	1.26×10^{-6}	2.12×10^{-6}	— [g]	— [g]	4.94×10^{-12}	4.56×10^{-12}	5.35×10^{-12}
9	73.5°	5.94×10^{-7}	1.78×10^{-6}	— [e]	— [e]	— [g]	— [g]	2.56×10^{-15}	2.25×10^{-15}	2.94×10^{-15}

[a]The uncertainty of each measured peak intensity is about 2% of the value.

[b]Values calculated from measured profiles using Eq. (19).

[c]Values calculated for a perfect sinusoid using Eq. (9).

[d]Values calculated for a perfect sinusoid using Eq. (21).

[e]Measured peak value obscured by the background.

[f]Diffracted peak obscured by instrument receiver.

[g]Computed peak value obscured by the background.

Table 2. Computed and Measured Power in the Peaks Relative to the Incident Power

Order	Computed[a] (95%)	Computed[a] (100%)	Computed[a] (105%)	Measured[b]	Measured[b]
−4	1.5×10^{-4}	2.2×10^{-4}	3.3×10^{-4}	4.84×10^{-4}	3.4×10^{-4}
−3	4.8×10^{-3}	6.2×10^{-3}	7.9×10^{-3}	— [c]	— [c]
−2	5.5×10^{-2}	6.3×10^{-2}	7.4×10^{-2}	— [c]	— [c]
−1	0.28	0.29	0.29	0.29	0.29
0	0.20	0.16	0.13	0.11	0.13
1	0.28	0.28	0.29	0.29	0.29
2	5.0×10^{-2}	5.9×10^{-2}	6.8×10^{-2}	7.9×10^{-2}	7.1×10^{-2}
3	4.3×10^{-3}	5.5×10^{-3}	7.0×10^{-3}	9.1×10^{-3}	7.4×10^{-3}
4	1.3×10^{-4}	2.0×10^{-4}	2.8×10^{-4}	4.5×10^{-4}	1.7×10^{-4}

[a]Calculated from scaled measured profiles of the aluminum sample using Eq. (19).

[b]Measured at different spots of the aluminum sample, s polarization.

[c]Diffracted peak obscured by instrument receiver.

Table 3. Background Scattering Ratio					
Scattering angle	15°	30°	45°	60°	75°
Computed ratio[a]	0.045	0.017	0.011	0.0090	0.0080
Measured ratio[b]	0.07	0.02	0.02	0.02	0.01

[a]Calculated from Eq. (42).

[b]Averages of ratios determined from Figs. 6 and 7 between values obtained from measured BRDF curves and those computed from measured profiles. The relative uncertainties in these comparisons are ~30%.

Figure Captions

Fig. 1. Diagram showing the sample configuration and the sign convention for the angles of the wavevectors of the incident and scattered waves.

Fig. 2. Partial profile of the aluminum-coated grating measured with a 1-µm tip and PSD of the full profile: (a) modified profile, (b) residual roughness computed from the Fourier transform of the profile, truncated below a spatial frequency of 0.33 μm^{-1}, and (c) and (d) the corresponding PSDs.

Fig. 3. Measured BRDF for the scattering of s- and p-polarized light by the aluminum sample. The peak power relative to the power in the specular peak is found in Table 1.

Fig. 4. Measured BRDF for the scattering of s- and p-polarized light by the gold sample. The peak power relative to the power in the specular peak is found in Table 1.

Fig. 5. Instrument signature.

Fig. 6. Measured BRDF (s polarization) and BRDF computed from measured profiles using the Kirchhoff approximation for the aluminum sample. The peak power relative to the power in the specular peak is found in Table 1.

Fig. 7. Measured BRDF (s polarization) and BRDF computed from measured profiles using the Kirchhoff approximation for the gold sample. The peak power relative to the power in the specular peak is found in Table 1.

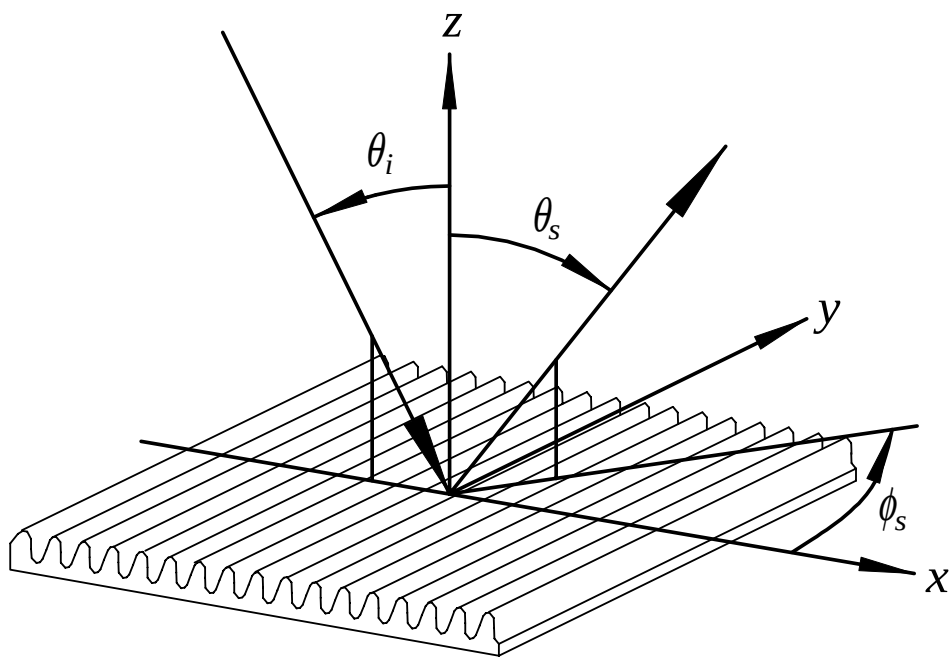

Fig. 1. Diagram showing the sample configuration and the sign convention for the angles of the wavevectors of the incident and scattered waves.

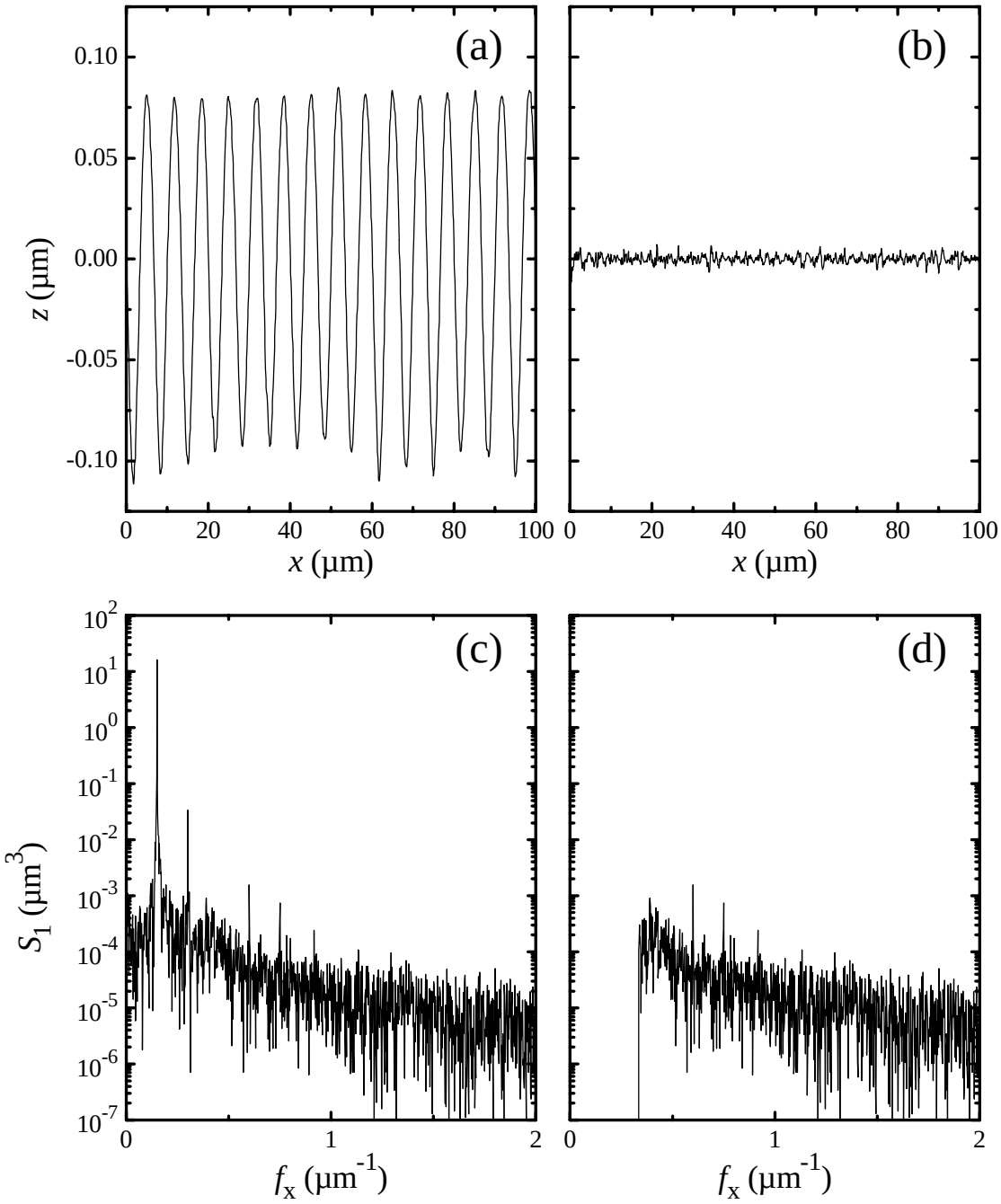

Fig. 2. Partial profile of the aluminum-coated grating measured with a 1-μm tip and PSD of the full profile: (a) modified profile, (b) residual roughness computed from the Fourier transform of the profile, truncated below a spatial frequency of 0.33 μm^{-1}, and (c) and (d) the corresponding PSDs.

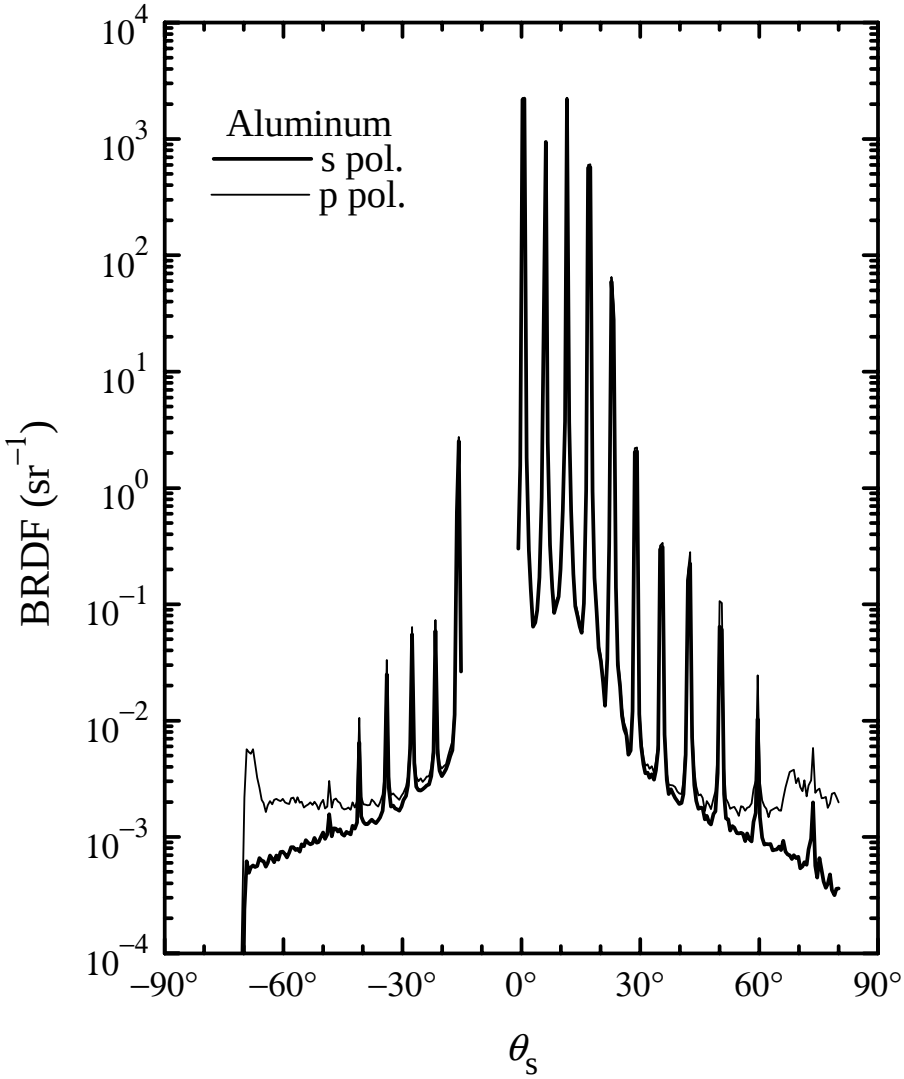

Fig. 3. Measured BRDF for the scattering of s- and p-polarized light by the aluminum sample. The peak power relative to the power in the specular peak is found in Table 1.

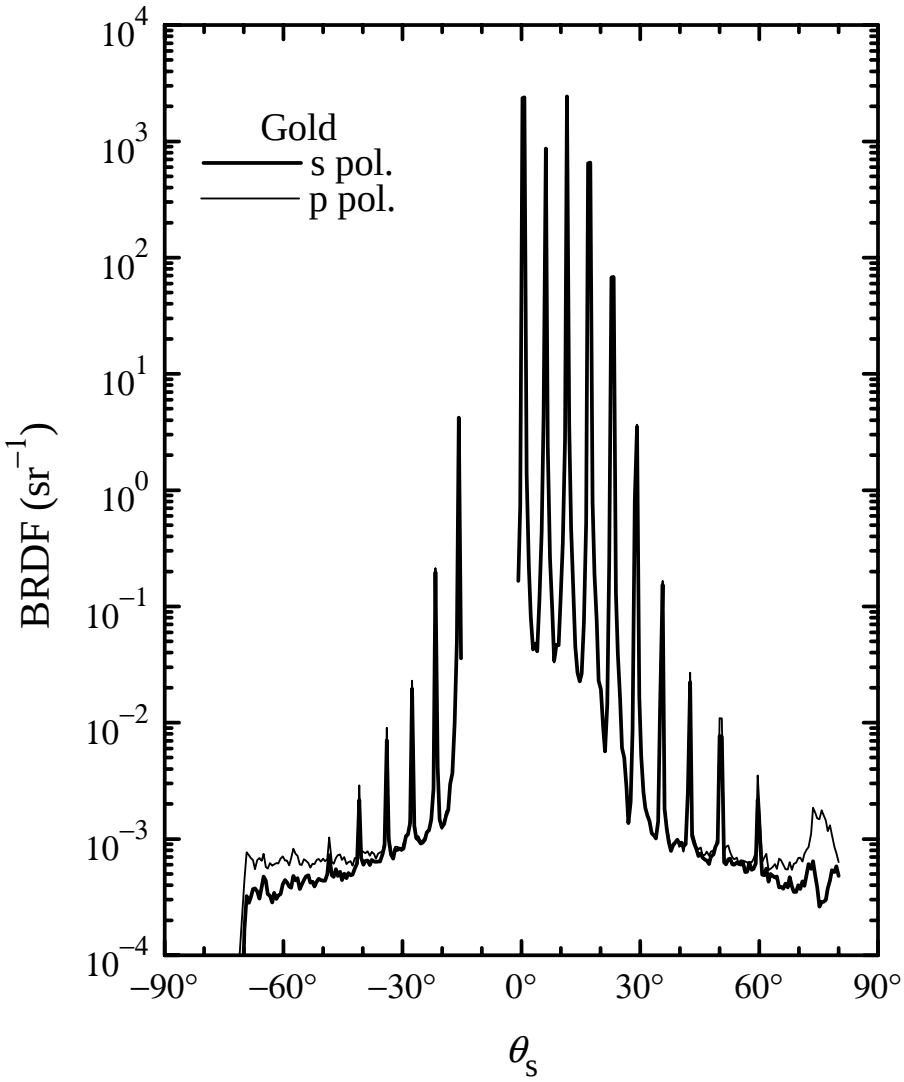

Fig. 4. Measured BRDF for the scattering of s- and p-polarized light by the gold sample. The peak power relative to the power in the specular peak is found in Table 1.

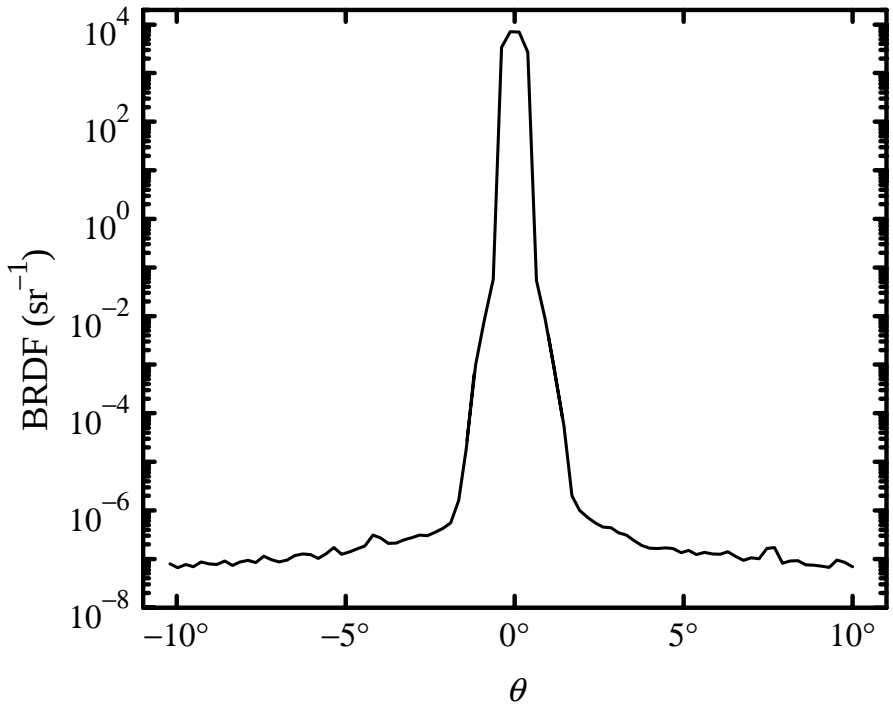

Fig. 5. Instrument signature.

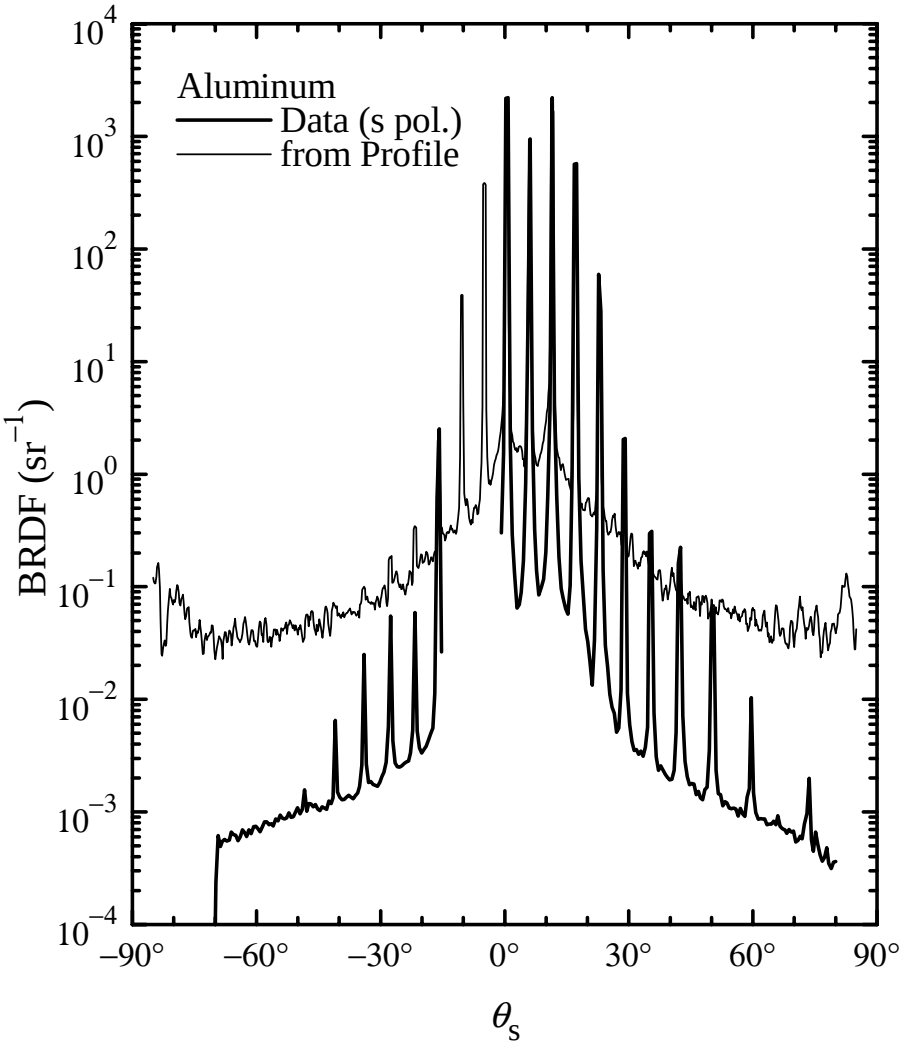

Fig. 6. Measured BRDF (s polarization) and BRDF computed from measured profiles using the Kirchhoff approximation for the aluminum sample. The peak power relative to the power in the specular peak is found in Table 1.

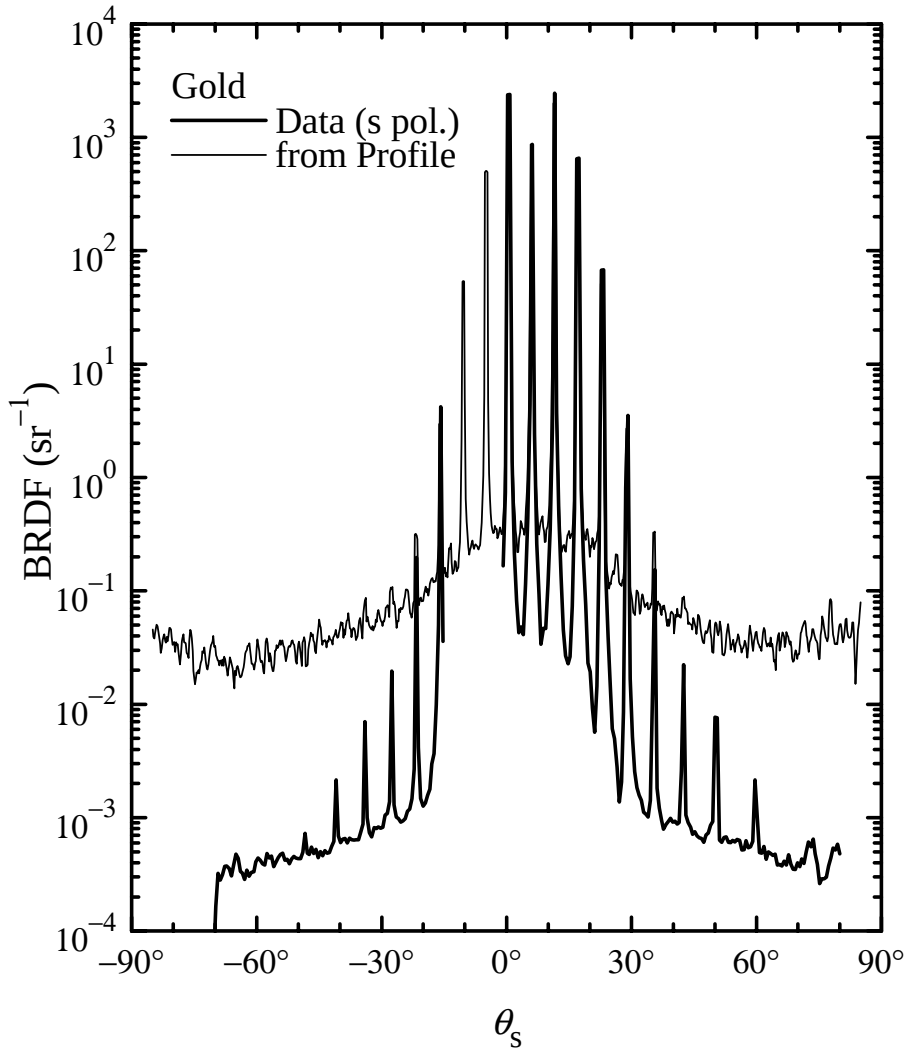

Fig. 7. Measured BRDF (s polarization) and BRDF computed from measured profiles using the Kirchhoff approximation for the gold sample. The peak power relative to the power in the specular peak is found in Table 1.